SCIENCE CHINA
Information Sciences

• RESEARCH PAPER •
Special Focus on Bistatic Synthetic Aperture Radar Signal Processing

June 2015, Vol. 58 062302:1–062302:14
doi: 10.1007/s11432-015-5320-z

Multichannel DEM reconstruction method based on Markov random fields for bistatic SAR

HONG Feng[1,2*], TANG JiangWen[1,2] & LU PingPing[1,2]

[1]*Institute of Electronics, Chinese Academy of Sciences(IECAS), Department of Space Microwave Remote Sensing System, Beijing* 100190*, China;*
[2]*University of Chinese Academy of Sciences, Beijing* 100049*, China*

Received February 1, 2015; accepted March 11, 2015; published online April 27, 2015

Abstract It appears very interesting and particularly useful to perform DEM reconstruction with the configuration of multichannel bistatic SAR (BiSAR) because of its considerable advantages. In typical processing flow of multichannel interferometric synthetic aperture radar (InSAR), techniques based on statistical methods or iterative methods does not work very well with limits of specific BiSAR configurations. Moreover, the tradeoff between the correctness and precision of the reconstruction of different baselines needs to be overcome as well. Based on the advantages of multichannel BiSAR configuration, basic idea is the joint utilization of amplitude data, iterative reconstruction results and ML results to help the optimization of the total MRF energy function. Thus, a multichannel DEM reconstruction method based on Markov Random Fields (MRFs) for BiSAR, which concerns much about discontinuities and energy functions, is proposed to achieve not only correct but also more precise results. Afterward, the strategy to determine the weight parameter and processing flow is presented. Finally, simulated and real data experiments are given to validate the proposed method.

Keywords interferometric synthetic aperture radar (InSAR), Markov random fields (MRFs), unwrapping, multichannel/multibaseline, bistatic SAR (BiSAR), digital elevation model (DEM)

Citation Hong F, Tang J W, Lu P P. Multichannel DEM reconstruction method based on Markov random fields for bistatic SAR. Sci China Inf Sci, 2015, 58: 062302(14), doi: 10.1007/s11432-015-5320-z

1 Introduction

The Bistatic Synthetic Aperture Radar (BiSAR) is characterized by separated transmitter and receiver, hence offering considerable capability, reliability, and flexibility in designing BiSAR missions [1,2]. Spaceborne/stationary bistatic SAR (SS-BiSAR) is a typical configuration of BiSAR, whose system geometry is shown in Figure 1. Under the situation of slide spotlight mode, the transmitter follows a rectilinear trajectory. Meanwhile, one synchronization receiver marked as in Figure 1 illuminates the satellite, and three echo receivers marked as E_1, E_2, E_3 in Figure 1 forming three baselines are fixed to the top of a high tower or mountain looking down to the illuminated scene which is marked as red area. It can perform interferometric applications by placing several receiving subsystems at slightly different positions on the high mountain in most case, thus allowing for instant urban monitoring for height profile measurements as well as subsidence detection and prediction. Such a system has many advantages, such as higher signal

* Corresponding author (email: hongfeng11@mails.ucas.ac.cn)

© Science China Press and Springer-Verlag Berlin Heidelberg 2015

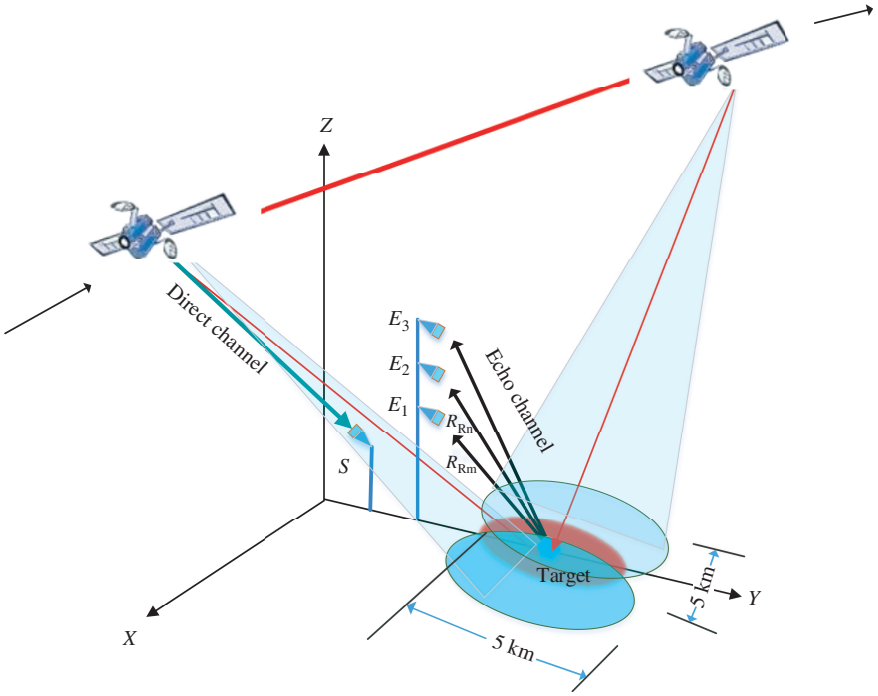

Figure 1 Typical configuration of multichannel BiSAR.

to noise ratio (SNR), relatively flexible design of baseline, and reduction of temporal decorrelation and atmospheric effects [3]. While the configuration of Multichannel SS-BiSAR has many advantages, some literatures have provided some experimental description or results [4–7].

DEM is related to the SAR interferometric phase through a known mapping, and it can be estimated by means of phase unwrapping (PhU)-based methods [8]. Single baseline PhU, mainly consists of two kinds of methods: path-following and minimum-norm methods [9]. The main difficulty is to derive the direct analytical solution for the inversion of the mapping from observed phases to unwrapped phases. In essence, the PhU is an ill-posed problem, unless proper regularity constraints are imposed. When the DEM of the observed scene is characterized by high slopes or exhibits strong height discontinuities, the DEM reconstruction obtained from a single interferogram is ambiguous, since the solution of the estimation problem is not unique [10]. For applications with the presence of buildings, the assumption is violated due to the presence of discontinuities and/or interferometric noise. We cannot get a correct solution due to the continuity assumption.

When more than one interferogram is available, a multibaseline approach allows us to overcome most of the difficulties encountered in InSAR DEM generation and to increase the final reconstruction accuracy. Combining multiple interferograms obtained with different baselines can solve the ambiguity and restore the solution uniqueness without imposing any constraints on the DEM. An improvement to the unwrapping step has been provided in the past fifteen years with the development of multichannel techniques, such as methods based on frequency division, wavelets methods, iterative methods, statistical methods and methods based on Chinese Remain Theory [11–19]. There exists some compromise between the correctness and precision of the DEM reconstructed with different baselines. DEM reconstructed with shorter baseline tends to allow higher error, while longer baselines cause greater phase unwrapping problems. Iterative methods [13] show that combining information from baselines of different lengths can take advantage of the greater accuracy of longer baselines while determining the phase wrapping from shorter baselines. In contrast, statistical methods like maximum likelihood (ML) [15] and maximum a posteriori (MAP) estimation [16], can be used for DEM reconstruction and have better characteristics. Generally, MAP techniques which take into account the relation between adjacent pixels outperform the ML techniques, and their attainable accuracy mainly depends on the ground slopes other than the choice of baselines [10]. Recently, some improved multibaseline reconstruction methods based on Markovian

approach are proposed [20,21]. Also, some other Markov random field (MRF) based algorithm used for single PhU or SAR image processing are also proposed in [22,23]. Among the different techniques developed in the multichannel framework, an interesting innovation has been provided in [16], authors provide an effective way to combine and jointly solve the PhU and regularization problem. In [20], authors propose an algorithm that is able to overcome some limitations of the methods named MRF-MAP in [16] regarding time computing and robustness to local optima in the optimization process. However, it has requirements of relatively large memory which constraints its function on large-scale application. In [22], the referred algorithm based on MRF does not focus on discontinuities and perform smoothness prior everywhere, partially for the lack of information when recovering single baseline phase.

Considering the characteristics and advantages of BiSAR configuration [24–26], this paper will focus on DEM reconstruction with the configuration of multichannel BiSAR for its advantages. Specifically, the advantage is once a time we can obtain twelve groups of receiving data at the most and more than fifty interferometric phase diagrams can be obtained. Therefore, the influence of the temporal decorrelation and the atmosphere effect on the interferometric results can be tremendously reduced. Additionally, the design and measurement of baseline is very flexible and precise without estimation, which is useful for improvement of the precision of reconstruction. Moreover, both the monostatic SAR (monoSAR) image and the multiple BiSAR images can help DEM reconstruction.

Besides the multiple interferograms, more information is available in multichannel BiSAR configuration. Thus, basic idea is the joint utilization of amplitude data, iterative reconstruction results and ML results to help the optimization of the total MRF energy function based on the advantages of multichannel BiSAR. Firstly, amplitude data and interferograms share the same discontinuities, particularly on buildings: building edges can be found in the same position both on the amplitude image and interferograms in some areas. Secondly, the ML techniques, not considering the neighboring relationship, still can preserve the discontinuity information. However, there still remains problem for each single method. For example, the amplitude data based on backscattering characteristic, influenced by SNR, cannot clearly indicate whether the object is a building in some case. Moreover, ML techniques, compared to MRF-MAP techniques, have unsatisfactory results for spikes and instabilities. Therefore, we set a new energy function and propose an improved method to ensure the correctness, to improve the precision and to reduce the optimal time.

The paper is organized as follows: Section 2 describes the improved MRF model, for single baseline and multibaseline cases, respectively. Afterward, in Section 3, we propose an algorithm to determine the weight parameters and then acquire the optimum solutions for the proposed MRF model. Furthermore, simulated and real data experiments in combination with corresponding performance analysis are presented in Section 4. Finally, the conclusion is drawn and the ongoing efforts are summarized in Section 5.

2 The improved MRF models

The improved MRF models for the case of single baseline and multibaseline are proposed in the following parts, respectively.

2.1 The case of single baseline

Before describing the improved MRF model for the case of single baseline, it is essential to introduce the physical model. The simplified mechanism of single-baseline InSAR wrapping is shown in Figure 2. Because of the nonlinearity of wrapping operator, the inverse solution of the observation process seems difficult to handle. However, two kinds of relationships between the true and observed phases can be found: the relationship between adjacent locations and the stochastic dependence between the observed and true phases. The former indicates the observation is only dependent on its own true phase, which means the true phases provide sufficient information to predict the observed phase. The latter shows that the conditional independence of the observed first-order adjacent location means that one true phase variable is conditionally independent with all others [22].

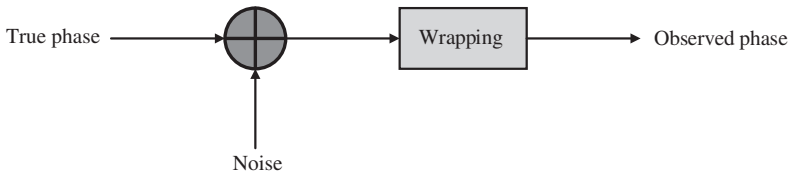

Figure 2 Simplified mechanism of single-baseline InSAR wrapping.

The improved energy function on each maximum clique for single channel reconstruction is given by

$$E(\Phi_{i,j}, D_{i,j\to i',j'}) = \sum_{i',j'\in N_{i,j}} (\omega_a^{i,j}(\Phi_{i,j} - \Phi_{i',j'})[1 - D_{i,j\to i',j'}] + \lambda \sum_{i,j} D_{i,j\to i',j'} + \omega_b^{i,j} g(\Phi_{i,j} - \varphi_{i,j})), \quad (1)$$

where $\Phi_{i,j}$ and $\varphi_{i,j}$ denotes the recovered phases and observed phases on site, $\Phi_{i',j'}$ denotes one of all other sites around site (i,j), $N_{i,j}$ denotes the first-order neighbors in the phase grid, $\omega_a^{i,j}$, λ and $\omega_b^{i,j}$ are weights helping to realize a trade-off between the three terms, $g(\cdot)$ is the introduced cost and $D_{i,j\to i',j'}$ is the line process vector which will be defined later. The first part of (1) represents the smoothness of the recovered phases, and the second part is the cost introduced by the discontinuities. For the first and second parts, we introduce a set of continuous line process vector $D_{i,j\to i',j'}$ into the smoothness term. The vector $D_{i,j\to i',j'}$, which contains four elements, works like a controller which has a "direction" for the site to determine whether the similarity between $\Phi_{i,j}$ and $\Phi_{i',j'}$ should be defined.

If a discontinuity is likely to be detected between site (i,j) and one of its neighboring sites, namely, (i',j'), the state is on and closer to $D_{i,j\to i',j'} = 1$; else, if the phase between the two points intends to be continuous and smooth, the state is off and closer to $D_{i,j\to i',j'} = 0$. The strategy of determination of vector $D_{i,j\to i',j'}$ will be described in Section 3. The last part of (1) represents the similarity between the recovered phases mod 2π and the observed phases. The total energy function of the MRF of single baseline case, which is non-convex due to $g(\cdot)$, is written as

$$\begin{aligned} &E_{\text{total}}(\boldsymbol{\Phi}, \boldsymbol{D}_{i,j\to i',j'}) \\ &\quad = \sum_{i,j} \sum_{i',j'\in N_{i,j}} (\omega_a^{i,j}(\Phi_{i,j} - \Phi_{i',j'})^2[1 - D_{i,j\to i',j'}] + \lambda \sum_{i,j} D_{i,j\to i',j'} + \omega_b^{i,j} g(\Phi_{i,j} - \varphi_{i,j})), \end{aligned} \quad (2)$$

where $\boldsymbol{\Phi}$ and $\boldsymbol{D}_{i,j\to i',j'}$ denote the vector forms of $\Phi_{i,j}$ and $D_{i,j\to i',j'}$. To get their corresponding estimations which are named as $\hat{\boldsymbol{\Phi}}$ and $\hat{\boldsymbol{D}}_{i,j\to i',j'}$, respectively, the total energy function in (2) is optimized by

$$\hat{\boldsymbol{\Phi}} = \arg\min_{\Phi} E_{\text{total}}(\boldsymbol{\Phi}, \boldsymbol{D}_{i,j\to i',j'}), \hat{\boldsymbol{D}} = \arg\min_{D} E_{\text{total}}(\boldsymbol{\Phi}, \boldsymbol{D}_{i,j\to i',j'}). \quad (3)$$

To a large extent, once the status of discontinuities is obtained, the heart of the work is completed. The strategy of figuring out which are discontinuities remains a vital part of the algorithm. Other work will be described in detail in Section 3.

2.2 The case of multibaseline

Before the improved MRF model for the case of multibaseline is proposed, we briefly introduce and analyze the general MRF model for multichannel DEM reconstruction. Authors propose a great solution to combine the interferograms to reconstruct the height of the observed scene within a Markovian framework [16]. Generally, the energy function contains two terms: the multichannel likelihood function and the a prior function. By using this approach, the height reconstruction problem becomes an energy minimization problem. The likelihood term takes the statistical distribution of the interferometric phases into account, while the a priori term puts some statistical constraints on the image to be reconstructed. The multichannel likelihood function given by [13]

$$F(\boldsymbol{\Psi}|\boldsymbol{h}) = \prod_{i,j\in S} \prod_{k} f(\varphi_{i,j}^{(k)}|h_{i,j}; h_a^{(k)}), \quad (4)$$

where $\boldsymbol{\Psi}$ and $\boldsymbol{h}$ denote the observed phases and true height vector, respectively, k denotes the channel number, $h_a^{(k)}$ denotes height ambiguity of channel k and $f(\varphi_{i,j}^{(k)}|h_{i,j};h_a^{(k)})$ denotes the conditional distribution of observed phases. The a priori model is based on MRFs, and its expression is given by

$$g(\boldsymbol{h};\eta)=\frac{1}{Z(\eta)}\mathrm{e}^{-E_{\mathrm{prior}}(\boldsymbol{h};\eta)}, \tag{5}$$

where $Z(\eta)$ is called the partition function used as a normalization factor, $E_{\mathrm{prior}}(\boldsymbol{h};\eta)$ is the prior energy function expressing the relationship between pixels, and η is the hyperparameter vector [21]. Following the Bayes law, the multichannel MAP estimation solution is given by

$$\hat{\boldsymbol{h}}=\arg\max F(\Psi|\boldsymbol{h})g(\boldsymbol{h};\eta). \tag{6}$$

Based on the analysis, we will propose the improved MRF model for the case of multibaseline. In practice, using interferograms with different baseline length can avoid the excessive dependence on the adjacent pixels with respect to the unwrapping problem, which helps to obtain better reconstruction results. For each site (i,j) in each interferogram, the linear relationship between the corresponding terrain height $h_{i,j}$ and unwrapped phase $\Phi_{i,j}$ is expressed as $h_{i,j}=h_a\cdot\Phi_{i,j}/2\pi$.

It is known that the observed phases of corresponding site on different interferograms originate from the same true terrain height. So the phase relationship of different interferograms can be obtained by the baseline with different length. Thus, a family of $C_K^2=(K(K-1)/2)$ equations are given as

$$h_a^{(l)}\Phi_{i,j}^{(l)}=h_a^{(k)}\Phi_{i,j}^{(k)},\quad l,k=1,2,\ldots,K(K-1)/2,\ l\neq k, \tag{7}$$

where $h_a^{(l)}$ and $h_a^{(k)}$ denote arbitrary different height ambiguity for different baselines, K denotes the number of echo antennas. Expanding (7), we can get

$$h_a^{(l)}\left(\varphi_{i,j}^{(l)}+2\pi m_{i,j}^{l}\right)=h_a^{(k)}\left(\varphi_{i,j}^{(k)}+2\pi m_{i,j}^{k}\right),\quad l,k=1,2,\ldots,K(K-1)/2,\ l\neq k, \tag{8}$$

where m denotes the fold time of absolute phase. The conditional distribution of observed phase is given by

$$\begin{aligned}f\left(\varphi_{i,j}^{(k)}|h_{i,j};h_a^{(k)}\right)=&\frac{1}{2\pi}\frac{1-|\gamma^{(k)}|^2}{1-|\gamma^{(k)}|^2\cos^2(\varphi_{i,j}^{(k)}-\frac{2\pi}{h_a^{(k)}}h_{i,j})}\\&\times\left\{1+\frac{|\gamma^{(k)}|\cos(\varphi_{i,j}^{(k)}-\frac{2\pi}{h_a^{(k)}}h_{i,j})\cos^{-1}[-|\gamma^{(k)}|\cos(\varphi_{i,j}^{(k)}-\frac{2\pi}{h_a^{(k)}}h_{i,j})]}{[1-|\gamma^{(k)}|^2\cos^2(\varphi_{i,j}^{(k)}-\frac{2\pi}{h_a^{(k)}}h_{i,j})]^{1/2}}\right\},\end{aligned} \tag{9}$$

where $\gamma^{(k)}$ is the coherence coefficient matrix of channel k, $\varphi_{i,j}^{(k)}$ is the observed phase on site (i,j) of channel k. In BiSAR fixed receiver multichannel case, height ambiguity is different with traditional expression, which can be derived as

$$h_a^{(k)}=\frac{\lambda(R_m(x_r,y_r,z_{\mathrm{ave}})+R_n(x_r,y_r,z_{\mathrm{ave}}))}{2B_k}, \tag{10}$$

where $R_m(x_r,y_r,z_{\mathrm{ave}})$ and $R_n(x_r,y_r,z_{\mathrm{ave}})$ are distances from the scene grid $(x_r,y_r,z_{\mathrm{ave}})$ to arbitrary two antennas, respectively, the average height of the scene is z_{ave}, λ is the wavelength and B_k is the kth baseline. As mentioned above, we can write the energy function on each maximal clique from the shortest baseline to longest baseline. For simplification, we just write the one of kth baseline as

$$\begin{aligned}&E^{(k)}\left(\Phi_{i,j},D_{i,j\to i',j'}^{(k)}\right)\\&=\sum_{i',j'\in N_{i,j}}\left(\omega_a^{i,j}(\Phi_{i,j}-\Phi_{i',j'})^2\left[1-D_{i,j\to i',j'}^{(k)}\right]+\lambda\sum_{i,j}D_{i,j\to i',j'}^{(k)}+\omega_b^{i,j}g\left(\phi_{i,j}/r^{(k)}-\varphi_{i,j}^{(k)}\right)\right),\end{aligned} \tag{11}$$

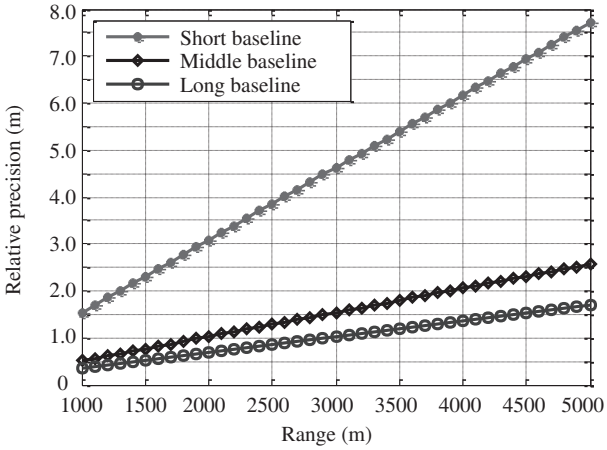

Figure 3 Relative precision of different baselines.

where r_k is the baseline ratio between different interferograms.

The relative precision for single-baseline bistatic InSAR is calculated as

$$\delta h_k = \frac{\lambda(R_m(x_r, y_r, z_{\text{ave}}) + R_n(x_r, y_r, z_{\text{ave}}))}{4B_k} \cdot \sigma, \tag{12}$$

where σ represents the standard deviation of the interferometric phase, and B_k is the length of the kth baseline. Figure 3 shows that different baselines have different precisions.

To sufficiently exploit the interferograms, the joint energy function on each maximal clique is built as

$$\begin{aligned} &E\left(\Phi_{i,j}, D^{(N)}_{i,j\to i',j'}\right) \\ &= \sum_{i',j'\in N_{i,j}} \left(\omega_a^{i,j}(\Phi_{i,j} - \Phi_{i',j'})^2 \left[1 - D^{(N)}_{i,j\to i',j'}\right] + \lambda \sum_{i,j} D^{(N)}_{i,j\to i',j'} + \omega_b^{i,j} \sum_k g\left(\phi_{i,j}/r^{(k)} - \varphi^{(k)}_{i,j}\right)\right), \end{aligned} \tag{13}$$

wherein $g(\phi, \varphi) = \frac{1}{4}|\mathrm{e}^{\mathrm{j}(\phi-\varphi)} - 1|^2$ and $\omega_b^{i,j}$ is the parameter used to control the sensitivity of the difference of the estimated unwrapped phase and the observed phase. While various kinds of formation can be selected [27], we choose the $g(\phi, \varphi)$ as the measurements of the similarity of the recovered phases ϕ and observed phases φ. Considering the periodical property of phases, such a choice indicates an expensive cost if ϕ and φ are opposite and a cheap cost if they are close. The last part of (13) is changed to keep the same precision order. Specifically, because the recovered and observed phases depend on baseline, $r^{(k)}$ is introduced to unify the recovered phases with the order of longest baseline, and definitely the highest precision. Therefore, the total energy function of the multichannel MRF is given by

$$\begin{aligned} E_{\text{total}}\left(\boldsymbol{\Phi}, \boldsymbol{D}^{(N)}_{i,j\to i',j'}\right) = \sum_{i,j} \sum_{i',j'\in N_{i,j}} &\left(\omega_a^{i,j}(\Phi_{i,j} - \Phi_{i',j'})^2 \left[1 - D^{(N)}_{i,j\to i',j'}\right]\right. \\ &\left. + \lambda \sum_{i,j} D^{(N)}_{i,j\to i',j'} + \omega_b^{i,j} \sum_k g\left(\phi_{i,j}/r^{(k)} - \varphi^{(k)}_{i,j}\right)\right). \end{aligned} \tag{14}$$

To get the estimations named as $\hat{\boldsymbol{\Phi}}$ and $\hat{\boldsymbol{D}}^{(N)}_{i,j\to i',j'}$,which are the unwrapped phase and state vector of the interferogram with highest precision,respectively, the total energy function $E_{\text{total}}(\boldsymbol{\Phi}, \boldsymbol{D}^{(N)}_{i,j\to i',j'})$ in (14) is optimized by

$$\langle \hat{\boldsymbol{\Phi}}, \hat{\boldsymbol{D}} \rangle = \arg\min_{\Phi, D} E_{\text{total}}(\boldsymbol{\Phi}, \boldsymbol{D}^{(N)}_{i,j\to i',j'}). \tag{15}$$

3 Realization of the algorithm

The realization of this algorithm can be implemented by the steps used in traditional MRF-MAP DEM reconstruction methods, which means there are frequent Expectation-Maximum (EM) calculations and Gibbs Sampling steps that need long-time calculation. Considering the aspect of speed of calculation, an optimization procedure has been adopted to accelerate the implementation. Because the update of hypermeters is directional, the steps will be more effective. The processing flow for this approach is shown in Figure 4.

3.1 Steps for the optimization of energy function

A detailed step by step list for optimization is as follows:

Step 1. Get initial height maps. Use the interferometric phase diagrams (IPD) of shortest baseline via traditional unwrapping method such as Minimum Cost Flow (MCF) to get h_s, and use multiple interferometric phase diagrams i.e., IPD_1, $\mathrm{IPD}_2, \ldots, \mathrm{IPD}_N$, to get h_{ML} and h_{iter} via stochastic and iterative methods, respectively.

Step 2. Feature normalization and differentiate. Before we differentiate $\boldsymbol{h}_{\mathrm{ML}}$ and $\boldsymbol{h}_{\mathrm{iter}}$ to get $\boldsymbol{h}_s$, feature normalization is necessary to keep the height map in the same scale. Feature normalization means removal of the expectation value of matrix $\boldsymbol{h}_{\mathrm{ML}}$ and $\boldsymbol{h}_{\mathrm{iter}}$.

Step 3. Calculate initial $\boldsymbol{D}_{i,j\to i',j'}$ and Assign weight parameters. To complete this step, assistant information like kth amplitude image $\mathbf{Amp}^{(k)}$ should be provided. The initial $\boldsymbol{D}_{i,j\to i',j'}$ is determined by both the gradient amplitude image $\nabla\mathbf{Amp}^{(k)}$ and differentiate height map $\boldsymbol{h}_\varepsilon$. Each vector $\nabla\mathrm{Amp}^{(k)}_{i,j\to i',j'} \in \nabla\mathbf{Amp}^{(k)}$ has a neighboring field of four elements. If the gradient differentiate height exceeds the corresponding height ambiguity and the gradient amplitude image vector exceeds the threshold, namely $|h_s| > h_a^{(k)}$ and $\nabla\mathrm{Amp}^{(k)}_{i,j\to i',j'} > \mathrm{TH}_A$, then $\boldsymbol{D}_{i,j\to i',j'} = 1$; else $\boldsymbol{D}_{i,j\to i',j'} = 0$. The physical model shows the symmetric property, which means $\boldsymbol{D}_{i,j\to i',j'} = \boldsymbol{D}_{i',j'\to i,j}$. Assign the weight parameters determined by the way shown in the next section.

Step 4. Update $\boldsymbol{D}_{i,j\to i',j'}$ and weight parameters. If the estimation of the height maps $\boldsymbol{h}_n$ has performed at least one time, then update $\boldsymbol{D}_{i,j\to i',j'}$. The only difference between this step and step 3 is substitute $\boldsymbol{h}_n$ with $\boldsymbol{h}_{\mathrm{iter}}$.

Step 5. Resolve the energy function with Iterative Condition Mode (ICM) and obtain the new height estimation h_n. This step is very similar like the mentioned MRF methods. Take h_n as the new initial condition, determine $\boldsymbol{D}_{i,j\to i',j'}$, and assign new weight parameters.

Step 6. Repeat 4 and 5 until the set condition $\mathrm{norm}(\boldsymbol{h}_n, \boldsymbol{h}_{n-1}) <$ Threshold is satisfied. The operation $\mathrm{norm}(\boldsymbol{h}_n, \boldsymbol{h}_{n-1})$ denotes $\sum_{i,j\in S}(\boldsymbol{h}_n - \boldsymbol{h}_{n-1})^2/N_{\mathrm{site}}$, which means the average summation of difference between $(n-1)$th and nth reconstruction results for all sites N_{site} with high coherence coefficient. The selection of the Threshold can be determined by an experience value, for example, $0.5\delta\widehat{h}$, where $\delta\widehat{h}$ denotes the average relative precision of the longest baseline.

Step 7. Obtain final results h_{est}. Solution of this algorithm focuses on the maximization of the posteriori energy. It may be very hard to solve, and thus instead we are trying to locally maximize every pixel because maximizing the total one is equal to maximizing the condition probability for its Markovianity. The ICM algorithm uses the greedy strategy in the iterative local maximization. Given the data $\varphi_{i,j}$ and other labels $\Phi_{S-i,j}$, the algorithm sequentially performs optimization and obtains the results as

$$P(\Phi_{i,j}|\varphi, \Phi_{S-\{i,j\}}) \propto P(\varphi_{i,j}|\Phi_{i,j})P(\Phi_{i,j}|\Phi_{N_{i,j}}), \tag{16}$$

with the rule

$$\Phi^{(k)}_{i,j} \leftarrow \arg\min_{\Phi_{i,j}} E\left(\Phi_{i,j}|\varphi_{i,j}, \Phi^{(k)}_{N_{i,j}}\right), \tag{17}$$

where $E(\Phi_{i,j}|\varphi_{i,j}, \Phi^{(k)}_{N_{i,j}})$ denotes the energy function of channel k.

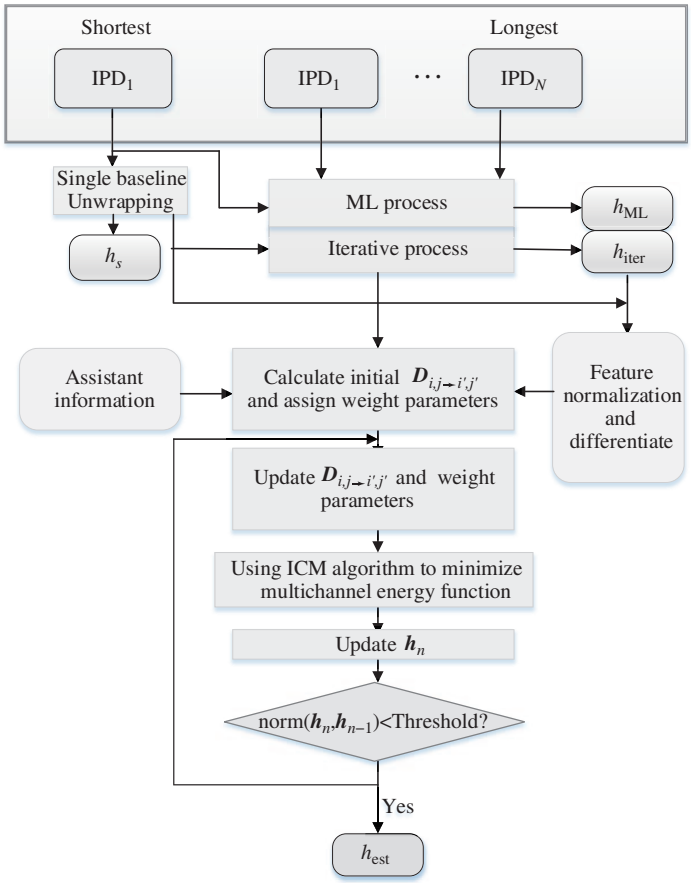

Figure 4 Processing flow for the proposed DEM strategy.

3.2 Parameters of weights

Weights selection in the algorithm also needs to be discussed. In general, we expect these three terms to play the same role when recovering true phase image. Thus, the parameter should make every part of the energy function to roughly be in the same scale. The values of weights should vary according to the characteristics and local changes of phase for specific applications. Here, a simple empirical way to assign these three parameters is offered. Then $\omega_a^{(i,j)}$ is defined as

$$\omega_a^{(i,j)} = \max\left\{\sum_{i',j'\in N_{i,j}} (\phi_{i,j}-\phi_{i',j'})^2\left[1-D^{(k)}_{i,j\to i',j'}\right]\right\}^2, \tag{18}$$

where $\omega_b^{i,j}$ is the weight of the closeness and determines the penalty for the difference between observed phase and recovered phase. When the coherence coefficient is lower, i.e., the observation phase is less reliable, we will assign less weights for that property. Similar to the quality-map approach, we set the value of $\omega_b^{i,j}$ as coherence coefficient $\gamma_{i,j}$ of each site (i,j), i.e.,

$$\omega_b^{i,j} = \gamma_{i,j}. \tag{19}$$

Finally, the discontinuities weight parameter $\lambda_{i,j\to i',j'}$, which determines the cost of the potential is assigned as

$$\lambda_{i,j\to i',j'} = \frac{1}{1+\mathrm{e}^{-(\mathrm{Amp}_{i,j}-\mathrm{Amp}_{i',j'})^2}}, \tag{20}$$

where $\mathrm{Amp}_{i,j}$ and $\mathrm{Amp}_{i',j'}$ are the amplitude value at site (i,j) and (i',j'), respectively.

Table 1 Simulation parameters

Parameter	Value	Parameter	Value
Incident angle (θ)	60°–87°	Ambiguity height (h_{a1})	21.4 m
Platform height (H)	250 m	Ambiguity height (h_{a2})	32.1 m
Signal wavelength (λ)	0.031 m	Ambiguity height (h_{a3})	53.5 m
Signal bandwidth ($\triangle$f)	100 MHz	SNR	13 dB
Channel numbers (K)	3		

4 Experiment

4.1 Simulated data experiment

The algorithm described in the previous section is tested first on simulated data, using the data originated from DEM of Isolation Peak (Colorado) with pixel size of 458×157. The simulated parameters are listed in Table 1.

The observed phases with longest, middle, and shortest baselines are shown in Figure 5 (a)–(c), respectively. It is obvious that the density of the fringe is proportional to effective baseline length. The true DEM information of Isolation Peak is presented in Figure 5(m). There exists an explicit cliff with the altitude difference of 137 m whose corresponding phase difference is 12.8π, 8.5π, and 5.1π, which certainly does not satisfy the continuity assumption. The cliff is marked with the dashed black box. To test the performance, we give the single baseline unwrapping results using MCF, one of the classical single baseline unwrapping method, from the corresponding baselines. We circle the interested area in each figure with black color. We can see the area marked by ellipsoid is considered continuous, thus leading to wrong results. It is obvious that traditional single unwrapping methods are not suitable for the case when the strong discontinuities exist, although it has a reliable performance in other area.

We also present the results and errors of ML, MAP and the proposed methods in Figure 5 (g)–(i) and Figure 5 (j)–(l), respectively. It appears that results obtained by ML methods can detect the discontinuous area but also have many spikes. In contrary, the performance of MAP is satisfactory in the blue area and the discontinuities are also detected. However, as marked in the yellow dashed circle, the area right to the discontinuous line, is partially not correctly reconstructed. The main error results from the right area and also the speed is unsatisfactory due to the steps of Gibbs sampling. Figure 5(l) shows the main error is generated in the cliff area due to the rapid change which leads to relatively lacking precision. The average error of ML, MAP, and our proposed method is 23.91, 0.73 and 0.58 m, respectively. The normalized RMS error is 0.63, 0.0229 and 0.0177, respectively. When it refers to the computational time, it is obvious that ML outperforms because its computational time is about 17.31 s. In contrast, MAP method consumes about 2600 s while our proposed method requires the average processing time of about 412 s. The proposed method is about five times faster than the MAP method, which corresponds with the analyses presented in Section 3. In overall perspective, the reconstruction results of our proposed methods are stable and satisfactory in the both the areas.

4.2 Real data experiment

The experiment is performed based on TerraSAR-X and the bistatic ground receivers. Our multi-channel BiSAR stationary receiver system includes the echo antenna group, direct antenna, radio frequency unit, data collection unit, and detection unit. The baseline length is designed as 0.8, 2.4, 3.2 m, respectively.

The experiment parameters are shown in Table 2.

The imaging algorithm is Back-projection Algorithm (BPA) accelerated by Graphic Processing Unit (GPU). The characteristics of BPA determine that the interferometric steps require no registration and flattening. One of the three BiSAR images is presented in Figure 6(a). The region of interest (ROI) is the building area with unavoidable discontinuities, whose enlarged scene of several buildings is given in Figure 6(b).

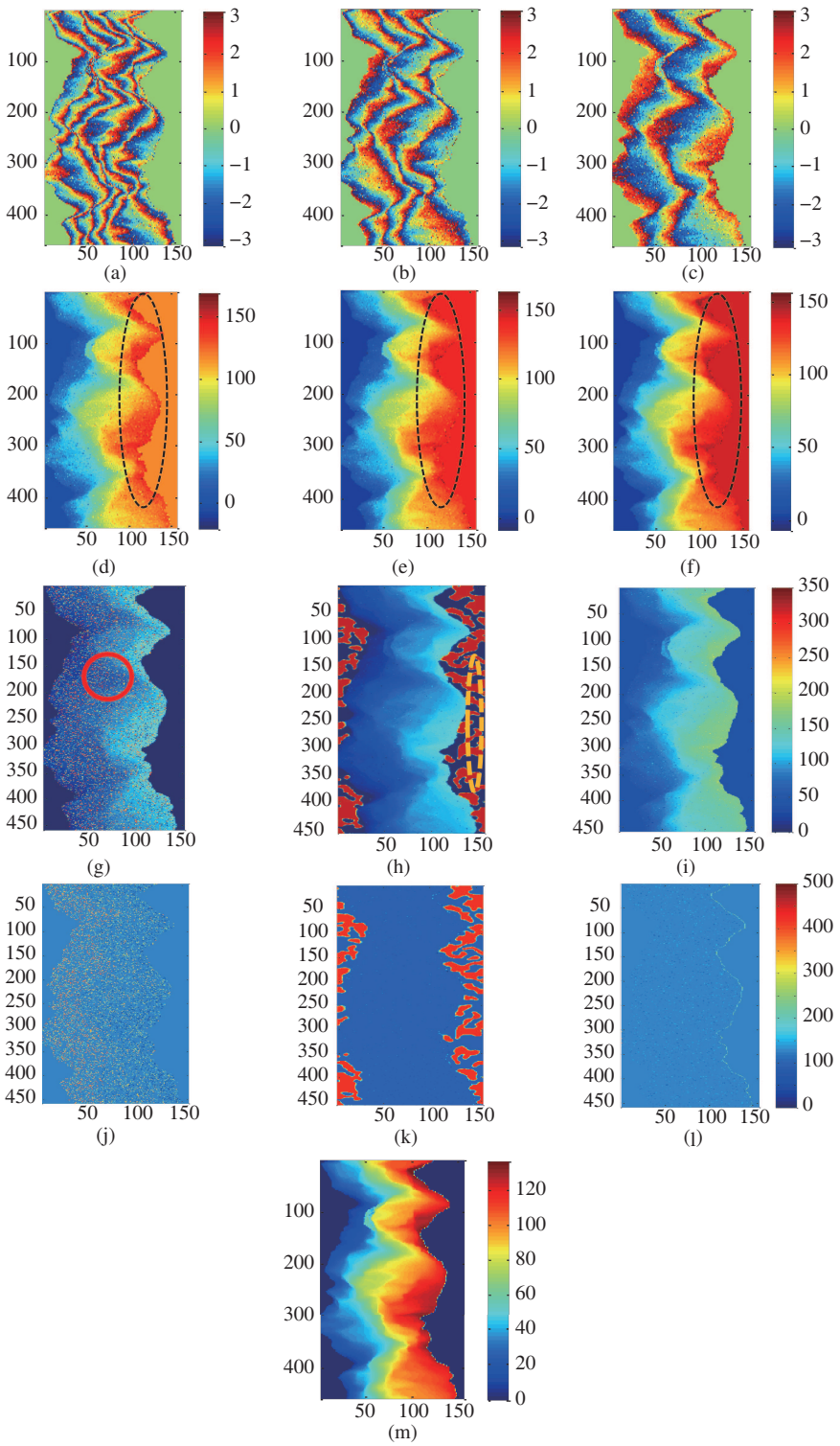

Figure 5 Results of simulated data experimental. (a)–(c) Observed phases with longest, middle, shortest baselines, respectively; (d)–(f) corresponding unwrapping phases with MCF method; (g)–(i) results of ML, MAP and our proposed methods; (j)–(l) error of ML, MAP and our proposed methods; (m) true DEM.

Height ambiguity of each baseline is given in Figure 7 (a)–(c). Since the geometric relationship is a little different, the looking angle changes rapidly, thus leading to the variant ambiguity height which changes with the value of range and cannot be simply approximated.

Figure 8 shows that the recovered phases will lead to over-smooth effect if ignoring discontinuities and

Table 2 Simulation parameters

Parameter	Value	Parameter	Value
Carrier frequency	9.65 GHz	Maximum height in scene	50 m
Signal bandwidth	300 MHz	Vertical baseline length	0.8 m, 2.4 m, 3.2 m
A/D sampling rate	725 MHz	Relative vertical height between antenna and scene	220 m
Average scene slant range for receiver	2000 m		

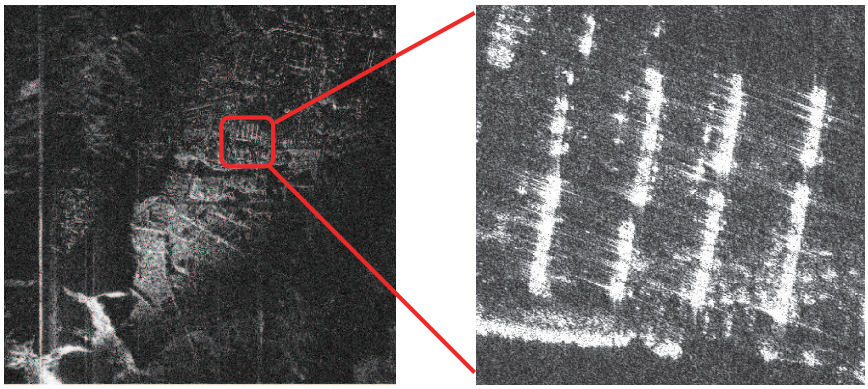

(a) (b)

Figure 6 BiSAR experimental results. (a) Whole scene SAR image; (b) interested area (building area).

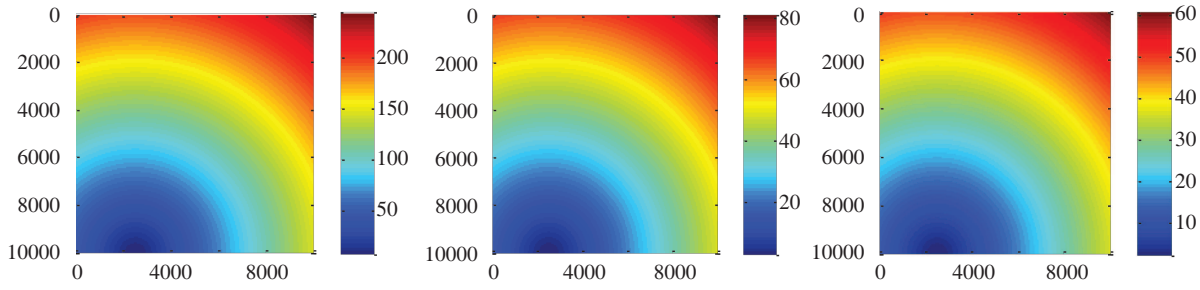

(a) (b) (c)

Figure 7 BiSAR experimental. (a)–(c) Height ambiguity of 0.8, 2.4, 3.2 m baseline, respectively.

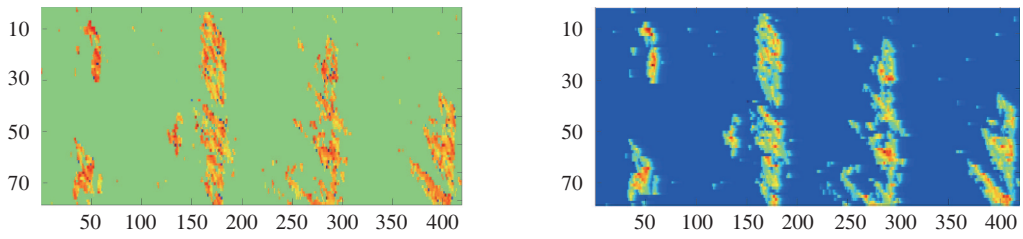

(a) (b)

Figure 8 Over-smooth effect when using MRF method proposed in [22] (part of reconstruction results of ROI), the x and y axis represents the direction of range and across-range of BiSAR. (a) Observed phase of baseline 2.4 m with the low coherence area filtered; (b) part of the reconstruction results of the MRF method proposed in [22].

using Markov method described in literature [22] to recover the wrapped phases.

The final results are given in Figure 9. Although the validity of this proposed strategy has been proved by error analysis for simulated data, validity for real experimental data is provided here. The ROI highlighted by red box shown in Figure 9(c) is the urban area located in Beijing. The sites with coherence coefficient lower than 0.7 are filtered in this case. The reconstruction results with ML, MAP method are shown in Figure 9 (a) and (b), respectively. It is shown many spikes are distributed in the

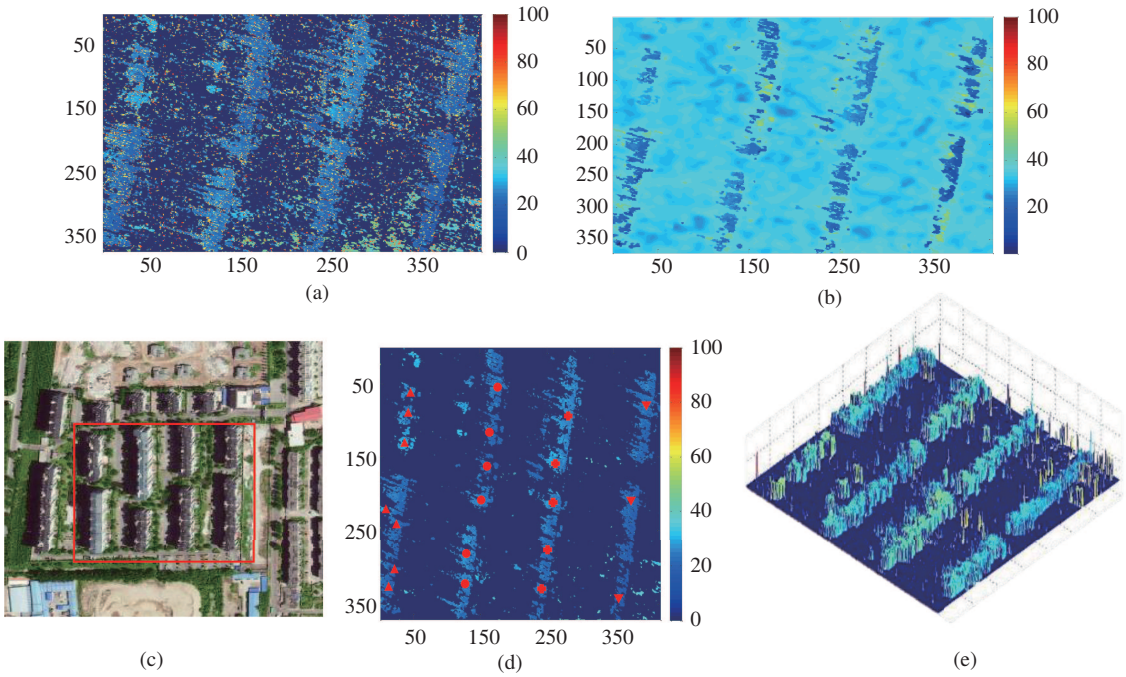

Figure 9 Final reconstruction results. (a) and (b) With ML, MRF-MAP method, respectively; (c) optical image of interesting area; (d) and (e) with our proposed methods of 2D and 3D perspective, respectively.

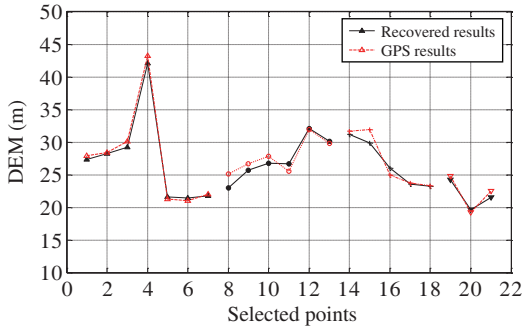

Figure 10 GPS and estimated DEM results of selected points.

whole scene which leads to incorrect results. In contrast, results obtained by MRF-MAP methods, which implement four times EM iteration and six times ICM iteration, are also not satisfactory. The area between buildings are obviously not satisfactory. Since there exists no DEM of state-of-art with high precision, we use GPS to take height measurements for twenty-one representative sites which are marked with red circles from up-to-down and left-to-right in Figure 9(d). The corresponding 3D view of the reconstruction result is given in Figure 9(e).

The comparison of recovered height with black color and GPS result with red color is shown in Figure 10. The four groups of selected points are marked with different marks, corresponding to Figure 9(b). The average error of ML, MAP, and our proposed method is 7.13, 1.73 and 0.98 m, respectively. The normalized RMS error of twenty-one selected sites reconstructed by ML, MAP methods, and the proposed method is 0.1072, 0.0335 and 0.014, respectively. The three methods consume about 2, 150 and 25 min, respectively. The results show that the proposed method is better than ML and MAP methods in the case of multichannel BiSAR configuration.

Moreover, considering the computational burden for large scenes, a general strategy is first to primarily classify the areas according to the corresponding topography. For relatively continuous areas such as mountains and farmland, using traditional single baseline PhU methods will reduce the computational time. In contrast, the proposed method is particularly suitable for DEM reconstruction of the discontin-

uous areas, such as urban areas. If the urban area is very large, an alternative to reduce the processing time is the acceleration of GPU. Generally, the block operation is important, which is necessary for parallel computation. Finally, the DEM reconstruction results can help the design of baselines in next few BiSAR experiments, which would enhance the precision of the DEM for using longer baseline.

5 Conclusion

Performing DEM reconstruction with the configuration of multichannel BiSAR has many advantages. Traditional MRF methods used for the PhU problems still have two problems to solve, i.e., how to apply this to multichannel case and keep the precision in the same order, and how to enhance the capability to detect the discontinuities which cannot be ignored in practical work. In this paper, we proposed a multichannel DEM reconstruction method based on MRF for BiSAR to solve these problems. Based on the advantages of multichannel BiSAR configuration, the techniques fully exploit the amplitude data, iterative reconstruction results and ML results to help the optimization of the total MRF energy function. It shows that the full information can help detect the discontinuities correctly, and also achieve reconstruction with higher precision. Also, this proposed approach has the advantage of requiring less calculation with traditional MRF-MAP methods. Especially for the case of BiSAR configuration, this new approach provides an interesting tool not only for DEM estimation, but for future baseline selection. More properly designed baselines may provide complementary information that can further improve the final result. Our future research issues will focus on the employment of a large number of baselines, which are also based on our BiSAR experiments.

Acknowledgements

This work was supported by National Natural Science Foundation of China (Grant No. 61422113), which is seen as a key item of this work. We wish to acknowledge insights and valuable discussions with Prof. WANG Yu Robert and Dr. SHAO YunFeng. We really wish to thank Mr. GUO Lei, Mr. WANG Wei, Mr. ZHAO Shuo, Mr. WANG JiLi, Mr. ZHANG Heng, Mr. ZHAO Tuan and Mr. WANG XiangYu for their efforts and tremendous helps. Finally, the authors must thank our colleagues, Mr. WU XiaYi, Mr. WANG KunYe, Dr. LIU Gang, Dr. WANG Nan, Miss. LUO XiuLian, Miss. LU PingPing and Miss LENG Ying for their important contributions to this work.

References

1 Loffeld O, Nies H, Peters V, et al. Models and useful relations for bistatic SAR processing. IEEE Trans Geosci Remote Sens, 2004, 42: 2031–2038
2 Krieger G, Moreira A, Spaceborne bi- and multistatic SAR: potential and challenges. IEE Proc-Radar Sonar Navig, 2006, 153: 184–198
3 Nies H, Behner F, Reuter S, et al. Polarimetric and interferometric applications in a bistatic hybrid SAR mode using Terrasar-X. In: Proceedings of Geoscience and Remote Sensing Symposium (IGARSS), Hawaii, 2010. 110–113
4 Duque S, López-Dekker P, Merlano J C, et al. Bistatic SAR along track interferometry with multiple fixed receivers. In: Proceedings of Geoscience and Remote Sensing Symposium (IGARSS), Hawaii, 2010. 4099–4102
5 Duque S, López-Dekker P, Mallorqui J J, et al. Experimental results with bistatic SAR tomography. In: Proceedings of Geoscience and Remote Sensing Symposium (IGARSS), Cape TOWN, 2009. II-37–II-40
6 Wang R, Deng Y, Zhang Z, et al. Double-channel bistatic SAR system with spaceborne illuminator for 2-D and 3-D SAR remote sensing. IEEE Trans Geosci Remote Sens, 2013, 51: 4496–4507
7 Walterscheid I, Espeter T, Brenner A R, et al. Bistatic SAR experiments with PAMIR and TerraSAR-X-setup, processing, and image results. IEEE Trans Geosci Remote Sens, 2010, 48: 3268–3279
8 Bamler R, Hartl P. Synthetic aperture radar interferometry. Inverse Probl, 1998, 14: R1–R54
9 Ghiglia D C, Pritt M D. Two-dimensional Phase Unwrapping: Theory, Algorithms, and Software. New York: Wiley, 1998
10 Ferraiuolo G, Meglio F, Pascazio V, et al. DEM reconstruction accuracy in multichannel SAR interferometry. IEEE Trans Geosci Remote Sens, 2009, 47: 191–201
11 Pascazio V, Schirinzi G. Estimation of terrain elevation by multifrequency interferometric wide band SAR data. IEEE Signal Process Lett, 2001, 8: 7–9

12 Ferretti A, Prati C, Rocca F. Multibaseline InSAR DEM reconstruction: the wavelet approach. IEEE Trans Geosci Remote Sens, 1999, 37: 705–715
13 Thompson D G, Robertson A E, Arnold D V, et al. Multi-baseline interferometric SAR for iterative height estimation. In: Proceedings of Geoscience and Remote Sensing Symposium (IGARSS), Hamburg, 1999. 251–253
14 Pascazio V, Schirinzi G. Multifrequency InSAR height reconstruction through maximum likelihood estimation of local planes parameters. IEEE Trans Image Process, 2002, 11: 1478–1489
15 Fornaro G, Monti Guarnieri A, Pauciullo A, et al. Maximum likelihood multi-baseline SAR interferometry. IEE Proc-Radar Sonar Navig, 2006, 153: 279–288
16 Ferraiuolo G, Pascazio V, Schirinzi G. Maximum a posteriori estimation of height profiles in InSAR imaging. IEEE Trans Geosci Remote Sens, 2004, 1: 66–70
17 Eineder M, Adam N. A maximum-likelihood estimator to simultaneously unwrap, geocode, and fuse SAR interferograms from different viewing geometries into one digital elevation model. IEEE Trans Geosci Remote Sens, 2005, 43: 24–36
18 Yuan Z H, Deng Y K, Li F. Multichannel InSAR DEM reconstruction through improved closed-form robust Chinese remainder theorem. IEEE Geosci Remote Sens Let, 2013, 10: 1314–1318
19 Ferraioli G, Ferraiuolo G, Pascazio V. Phase-offset estimation in multichannel SAR interferometry. IEEE Geosci Remote Sens Lett, 2008, 5: 458–462
20 Ferraioli G, Shabou A, Tupin F, et al. Multichannel phase unwrapping with graph-cuts. IEEE Geosci Remote Sens Lett, 2009, 6: 562–566
21 Shabou A, Baselice F, Ferraioli G. Urban digital elevation model reconstruction using very high resolution multichannel InSAR data. IEEE Trans Geosci Remote Sens, 2012, 50: 4748–4758
22 Chen R P, Yu W D, Wang R, et al. Integrated denoising and unwrapping of InSAR phase based on Markov random fields. IEEE Trans Geosci Remote Sens, 2013, 51: 4473–4485
23 Denis L, Tupin L, Darbon J, et al. SAR image regularization with fast approximate discrete minimization. IEEE Trans Image Process, 2009, 18: 1588–1600
24 Shao Y, Wang R, Deng Y K, et al. Error analysis of bistatic SAR imaging and stereoscopy bistatic SAR. IEEE Trans Geosci Remote Sens, 2013, 51: 4518–4543
25 Wang R, Loffeld O, Neo Y L, et al. Focusing bistatic SAR data in airborne/stationary configuration. IEEE Trans Geosci Remote Sens, 2010, 48: 452–465
26 Wang R, Loffeld O, Nies H, et al. Frequency-domain bistatic SAR processing for spaceborne/airborne configuration. IEEE Trans Aero Elect Syst, 2010, 46: 1329–1345
27 Li S Z. Markov Random Field Modeling in Image Analysis. New York: Springer-Verlag, 2009. 126–129